

## GENERALIZATION OF THE LAST SCATTERING APPROXIMATION FOR THE SECOND SOLAR SPECTRUM MODELING: THE Ca I 4227 Å LINE AS A CASE STUDY

L. S. ANUSHA<sup>1</sup>, K. N. NAGENDRA<sup>1</sup>, J. O. STENFLO<sup>2,3</sup>, M. BIANDA<sup>3</sup>, M. SAMPOORNA<sup>1</sup>, H. FRISCH<sup>4</sup>, R. HOLZREUTER<sup>2,5</sup>,  
AND R. RAMELLI<sup>3</sup>

<sup>1</sup> Indian Institute of Astrophysics, Koramangala, Bangalore 560 034, India

<sup>2</sup> Institute of Astronomy, ETH Zürich, CH-8093 Zürich, Switzerland

<sup>3</sup> Istituto Ricerche Solari Locarno, Via Patocchi, 6605 Locarno-Monti, Switzerland

<sup>4</sup> UNS, CNRS, OCA, Laboratoire Cassiopée, F-06304, Nice Cedex, France

<sup>5</sup> MPI für Sonnensystemforschung, D-37191 Katlenburg-Lindau, Germany

Received 2010 April 16; accepted 2010 May 31; published 2010 July 9

### ABSTRACT

To model the second solar spectrum (the linearly polarized spectrum of the Sun that is due to coherent scattering processes), one needs to solve the polarized radiative transfer (RT) equation. For strong resonance lines, partial frequency redistribution (PRD) effects must be accounted for, which make the problem computationally demanding. The “last scattering approximation” (LSA) is a concept that has been introduced to make this highly complex problem more tractable. An earlier application of a simple LSA version could successfully model the wings of the strong Ca I 4227 Å resonance line in Stokes  $Q/I$  (fractional linear polarization), but completely failed to reproduce the observed  $Q/I$  peak in the line core. Since the magnetic field signatures from the Hanle effect only occur in the line core, we need to generalize the existing LSA approach if it is to be useful for the diagnostics of chromospheric and turbulent magnetic fields. In this paper, we explore three different approximation levels for LSA and compare each of them with the benchmark represented by the solution of the full polarized RT, including PRD effects. The simplest approximation level is LSA-1, which uses the observed center-to-limb variation of the intensity profile to obtain the anisotropy of the radiation field at the surface, without solving any transfer equation. In contrast, the next two approximation levels use the solution of the unpolarized transfer equation to derive the anisotropy of the incident radiation field and use it as an input. In the case of LSA-2, the anisotropy at level  $\tau_\lambda = \mu$ , the atmospheric level from which an observed photon is most likely to originate, is used. LSA-3, on the other hand, makes use of the full depth dependence of the radiation anisotropy. The  $Q/I$  formula for LSA-3 is obtained by keeping the first term in a series expansion of the  $Q$ -source function in powers of the mean number of scattering events. Computationally, LSA-1 is 21 times faster than LSA-2, which is 5 times faster than the more general LSA-3, which itself is 8 times faster than the polarized RT approach. A comparison of the calculated  $Q/I$  spectra with the RT benchmark shows excellent agreement for LSA-3, including good modeling of the  $Q/I$  core region with its PRD effects. In contrast, both LSA-1 and LSA-2 fail to model the core region. The RT and LSA-3 approaches are then applied to model the recently observed  $Q/I$  profile of the Ca I 4227 Å line in quiet regions of the Sun. Apart from a global scale factor both give a very good fit to the  $Q/I$  spectra for all the wavelengths, including the core peak and blend line depolarizations. We conclude that LSA-3 is an excellent substitute for the full polarized RT and can be used to interpret the second solar spectrum, including the Hanle effect with PRD. It also allows the techniques developed for unpolarized three-dimensional RT to be applied to the modeling of the second solar spectrum.

*Key words:* line: formation – magnetic fields – polarization – scattering – Sun: atmosphere

### 1. INTRODUCTION

The Ca I 4227 Å line shows the largest degree of linear polarization in the second solar spectrum (the linearly polarized spectrum of the Sun that is due to coherent scattering processes). The Hanle effect, a magnetic field modification of this linear polarization, was first observed on the Sun in the core of this line by Stenflo (1982). Enigmatic behaviors of the line wing polarization were observed not only in active regions (see Bianda et al. 2003) but also in the quiet regions of the Sun (see Sampoorna et al. 2009, hereafter S09). These observations motivated the modeling of the Ca I 4227 Å line by an extension of the last scattering approximation (LSA) method, originally formulated by Stenflo (1982). It is shown in S09 that the unexpected wing features cannot be interpreted in terms of the Hanle effect, which was thought to become operative in the line wings through a combination of frequency redistribution and elastic collisions (Nagendra et al. 2002; Sampoorna et al. 2007).

The idea behind the LSA introduced in Stenflo (1982) is that the observed polarization  $Q/I$  can be evaluated by considering only one single scattering process in which the observed Stokes  $I$  plays the role of the incident radiation field. Its center-to-limb variation (CLV) provides the angular distribution needed to calculate the anisotropy of the radiation field which is the ultimate source of linear polarization. The purpose of LSA-type methods is to derive the linear polarization from Stokes  $I$ , avoiding the solution of the full scale polarized radiative transfer (RT) equation which is always somewhat computationally expensive and may still be beyond the capabilities of existing computers; for example, if one deals with three-dimensional calculations.

The modeling strategy in S09 is based on an extension of the LSA method introduced in Stenflo (1982) for frequency coherent scattering (incident and scattered beams have the same frequency). For the analysis of the Ca I 4227 Å line, frequency changes at each scattering are taken into account. They are described by an angle-dependent Hanle–Zeeman

partial frequency redistribution (PRD) matrix. In addition, the anisotropy of the radiation field is made frequency dependent. It is deduced from the CLV of Stokes  $I$  at a set of wavelengths along the intensity profile. With this procedure, it is possible to model the observed  $Q/I$  profile in the far line wings and the characteristic maxima of  $Q/I$  in the near line wings. However, the other features of the  $Q/I$  profile (the line center peak itself and the core minima) cannot be reproduced. The PRD matrix used in S09 provides a good representation of the frequency redistribution in the line core and the line wings and hence cannot be held responsible for the failure of the modeling at the line center. So we embarked on the construction of new LSAs which can take into account RT effects that are neglected when the polarization is deduced from the observed intensity only.

In this paper, we present three different LSAs. For clarity, we refer to them as LSA-1, LSA-2, and LSA-3. LSA-3 and LSA-2 take into account RT effects, LSA-2 being a degraded version of LSA-3. LSA-3 is very similar to the single scattering approximation introduced in Frisch et al. (2009). LSA-1 is very similar to the LSA used in S09. All these approximations are computationally much faster than a full polarized RT calculation.

We validate the performance of LSA-1 to LSA-3 by comparing their predictions for the ratio  $Q/I$  of the Ca I 4227 Å line with the solution of a full polarized RT equation, which we refer to as the RT approach for brevity. For the RT approach, we use the numerical code developed by D. Fluri (see, e.g., Fluri et al. 2003; Holzreuter et al. 2005), which can take into account multilevel atoms and solar atmospheric models. We also compare the predictions of the LSA-3 and of RT calculations with recent observations of the Ca I 4227 Å line taken at IRSOL in 2010 January. With both methods, we can fit the triplet peak structure of the  $Q/I$  profile present around the line center rather well. A qualitative explanation for this triplet structure, observed in strong chromospheric lines such as Ca I 4227 Å and Na I D<sub>2</sub> 5890 Å (see Gandorfer 2000, 2002, 2005), can be found in Holzreuter et al. (2005). For comparison with observations, we have incorporated the effect of a microturbulent magnetic field in the LSA-3 approximation and RT calculation. It is a very straightforward generalization (see, e.g., Faurobert-Scholl 1993, 1994; Holzreuter et al. 2006). We note that all the approximations presented in this paper can be generalized to the case of the Hanle effect due to an oriented field (i.e.,  $U \neq 0$ ).

In Section 2, we present the polarized RT equations, which serve as a starting point for the RT approach and the LSA-3 and LSA-2 approximations. In Section 3, we describe the observations and the solar atmospheric models that are used for testing the RT calculation and the LSA-3 approximation. In Section 4, we briefly discuss the wavelength and depth dependence of the radiation field anisotropy. The basic equations of LSA-1, LSA-2, and LSA-3 are given in Section 5. Section 6 is devoted to comparisons between  $Q/I$  profiles calculated with the LSA-3 approximation and a full RT approach and also to comparisons with observations. The conclusions are presented in Section 7. A brief discussion on PRD matrices is given in the Appendix.

## 2. THE RADIATIVE TRANSFER APPROACH

Throughout this paper, we use the standard notation of line formation theory (Mihalas 1978; Stenflo 1994). Since we work with solar model atmospheres, all the physical quantities explicitly depend on the altitude  $z$  in the atmosphere. The polarized RT equation in a one-dimensional planar axisymmetric medium

is written in standard notation as

$$\mu \frac{\partial \mathbf{I}(\lambda, \mu, z)}{\partial z} = -[\kappa_l(z)\phi(\lambda, z) + \kappa_c(\lambda, z) + \sigma_c(\lambda, z)]\mathbf{I}(\lambda, \mu, z) - \mathbf{S}(\lambda, \mu, z), \quad (1)$$

where the Stokes vector  $\mathbf{I} = (I, Q)^T$ . The Voigt profile function is denoted by  $\phi$ . The dependence of  $\phi$  on  $z$  comes from the damping parameter  $a = \Gamma_{\text{tot}}/4\pi\Delta\nu_D$ . The radiative and collisional broadening are included in  $\Gamma_{\text{tot}}$ . The Doppler width is  $\Delta\nu_D = \sqrt{2k_B T/M_a + v_{\text{turb}}^2}/\lambda_0$ , where  $k_B$  is the Boltzmann constant,  $T$  is the temperature,  $M_a$  is the mass of the atom, and  $v_{\text{turb}}$  is the magnitude of the microturbulent velocity. Further,  $\kappa_l$  is the line-averaged absorption coefficient and  $\sigma_c$  and  $\kappa_c$  are the continuum scattering and continuum absorption coefficients, respectively. The total opacity coefficient is  $\kappa_{\text{tot}}(\lambda, z) = \kappa_l(z)\phi(\lambda, z) + \sigma_c(\lambda, z) + \kappa_c(\lambda, z)$ . In a two-level atom model with unpolarized ground level, the total source vector  $\mathbf{S} = (S_I, S_Q)^T$  is defined as

$$\mathbf{S}(\lambda, \mu, z) = \frac{\kappa_l(z)\phi(\lambda, z)\mathbf{S}_I(\lambda, \mu, z)}{\kappa_{\text{tot}}(\lambda, z)} + \frac{\sigma_c(\lambda, z)\mathbf{S}_c(\lambda, \mu, z) + \kappa_c(\lambda, z)\mathbf{B}(\lambda, z)}{\kappa_{\text{tot}}(\lambda, z)}. \quad (2)$$

Here  $\mathbf{B} = (B_\lambda, 0)^T$ , with  $B_\lambda$  being the Planck function at the line center wavelength.  $\mu = \cos\theta$ , with  $\theta$  being the co-latitude with respect to the atmospheric normal. The line source vector  $\mathbf{S}_I = (S_{I,l}, S_{Q,l})^T$  is given by

$$S_I(\lambda, \mu, z) = \frac{1-\epsilon}{\phi(\lambda, z)} \int_{-1}^{+1} \frac{d\mu'}{2} \int_0^\infty d\lambda' \hat{\mathbf{R}}(\lambda, \lambda', \mu, \mu', z) \mathbf{I}(\lambda', \mu', z) + \epsilon \mathbf{B}(\lambda, z). \quad (3)$$

Here, the redistribution matrix  $\hat{\mathbf{R}}(\lambda, \lambda', \mu, \mu', z)$  is the angle-averaged Domke–Hubeny PRD matrix for the non-magnetic scattering as given in Equation (A7) of the Appendix. The thermalization parameter  $\epsilon$  is defined by  $\epsilon = \Gamma_I/(\Gamma_R + \Gamma_I)$ , where  $\Gamma_R$  and  $\Gamma_I$  are, respectively, the radiative and inelastic collision rates. In Equation (3),  $(\lambda', \mu')$  refer to the incoming ray and  $(\lambda, \mu)$  refer to the outgoing ray.

The scattering part of the continuum source vector  $\mathbf{S}_c = (S_{I,c}, S_{Q,c})^T$  is defined by

$$S_c(\lambda, \mu, z) = \int_{-1}^{+1} \frac{d\mu'}{2} \hat{\mathbf{P}}_R(\mu, \mu') \mathbf{I}(\lambda, \mu', z), \quad (4)$$

where  $\hat{\mathbf{P}}_R$  is the Rayleigh phase matrix defined in the Appendix. For simplicity, frequency coherent scattering is assumed in the continuum. We define the total optical depth scale as  $d\tau_\lambda = -\kappa_{\text{tot}}(\lambda, z)dz$ . The formal solution of Equation (1) can be written as

$$\mathbf{I}(\lambda, \mu, \tau_\lambda) = \mathbf{I}_0(\lambda, \mu, T_\lambda) \exp\left[-\left(\frac{T_\lambda - \tau_\lambda}{\mu}\right)\right] + \int_{\tau_\lambda}^{T_\lambda} \exp\left[-\left(\frac{\tau'_\lambda - \tau_\lambda}{\mu}\right)\right] \mathbf{S}(\lambda, \mu, \tau'_\lambda) \frac{d\tau'_\lambda}{\mu} \quad (5)$$

for  $\mu > 0$ , and

$$\mathbf{I}(\lambda, \mu, \tau_\lambda) = \mathbf{I}_0(\lambda, \mu, 0) \exp\left(-\frac{\tau_\lambda}{\mu}\right) - \int_0^{\tau_\lambda} \exp\left[-\left(\frac{\tau'_\lambda - \tau_\lambda}{\mu}\right)\right] \mathbf{S}(\lambda, \mu, \tau'_\lambda) \frac{d\tau'_\lambda}{\mu} \quad (6)$$

for  $\mu < 0$ . Here,  $T_\lambda$  represents the monochromatic total optical depth in the medium. In the above equations,  $I_0$  is a radiation field incident on the medium. At the lower boundary,  $I_0(\lambda, \mu, T_\lambda) = (B_\lambda(T_\lambda), 0)^T$ . We assume that no radiation is incident on the upper free boundary ( $\tau_\lambda = 0$ ). Equations (1)–(6) are used in Section 5 to construct three different levels of LSA and to compute the polarized spectrum  $I(\lambda, \mu, \tau_\lambda)$ .

The polarized spectrum is calculated by a two-stage process described in Holzreuter et al. (2005). In the first stage, a multilevel PRD-capable Multilevel Approximate Lambda Iteration (MALI) code of Uitenbroek (2001; hereafter referred to as the RH-code) solves the statistical equilibrium equation and the unpolarized RT equation self-consistently and iteratively. The RH-code is used to compute the intensity, opacities, and collision rates. The angle-averaged redistribution functions of Hummer (1962) are used in the RH-code. In the second stage, the opacities and the collision rates are kept fixed, and the Stokes vector  $(I, Q)^T$  is computed perturbatively by solving the polarized transfer equation with the same angle-averaged redistribution functions as in the RH-code. For simplicity, in this stage a two-level atomic model is assumed for the particular transition of interest. Such a two-stage approach is justified when the degree of linear polarization is small, so that it does not affect the population of the levels under consideration. A perturbation technique of this type is used in Faurobert (1987) and Nagendra et al. (2002) for isothermal atmospheres, and is shown to work well. In Section 6, we present the theoretical model profiles of  $(I, Q/I)$  computed by the RT approach.

### 3. OBSERVATIONAL DETAILS AND SOLAR MODEL ATMOSPHERES

#### 3.1. The Observation of $(I, Q/I)$ in the Ca I 4227 Å Line

The data acquisition was done using the ZIMPOL-2 polarimeter (Gandorfer et al. 2004) at IRSOL in Switzerland. For details of the instrumentation facilities used for obtaining the results shown in this paper, see Bianda et al. (2009). As several details related to the data acquisition are given in S09, we do not elaborate them here.

Figure 1 shows the observations taken during 2010 January near the solar north pole (about 6'' inside the limb around spatial position 60''). The spectrograph slit was 60  $\mu\text{m}$  wide (0'5 wide on the disk) and 190'' long. The resulting CCD images are 140 pixels high in the spatial direction, with a pixel corresponding to 1'35, and 770 pixels wide in the wavelength direction, with a pixel corresponding to 5.3 mÅ. The total exposure time was 10 minutes (120 single recordings of 5 s each).

Figures 7(a) and (c) show the intensity and the  $Q/I$  profiles obtained by averaging the Stokes  $I$  and Stokes  $Q/I$  images in Figure 1 over the spatial interval 13''–41'' where the average distance from the limb corresponds to a value  $\mu = 0.1$ . The limb distance is calculated with the help of slit-jaw images registered during the integration time. Note that due to seeing effects the position of the limb oscillates with an rms of 1'1 which corresponds to an rms of about 0.011 in  $\mu$ .

The intensity image shows the broad line of Ca I at 4227 Å, which is nearly 90% saturated at the line center, with broad wings interspersed by the blend lines (see also the dotted line in Figure 7(a)). The polarization signatures seen in  $Q/I$  are due to resonance scattering. Especially worth noting are the PRD peaks (at  $\lambda \approx 4226.2$  Å and  $\lambda \approx 4227.1$  Å) with unequal heights in the near wings and the depolarization of  $Q/I$  at the

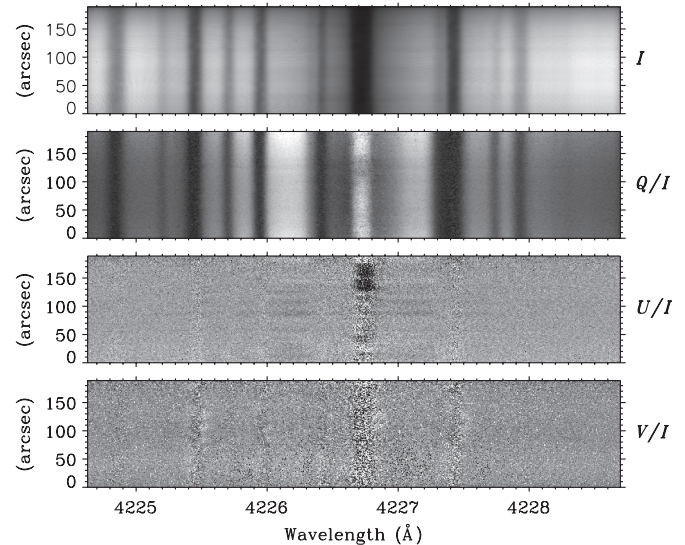


**Figure 1.** CCD image of the Stokes parameters in a spectral window around the Ca I 4227 Å line. The observations are made with the spectrograph slit placed parallel to the north limb (about 6'' inside around the spatial position 60''). Due to the curvature of the solar limb, the end points of the slit are closer to the limb when compared to the center of the slit. This explains the decrease in intensity and increase in the wing amplitude of  $Q/I$  when moving away from the center of the slit. In addition, seeing and guiding cause the image to oscillate and thus the distance of the limb from the spectrograph slit changes continuously. When recording an image, we average the measurements from different  $\mu$  values. In our case, the averaged value  $\mu = 0.1$  has an rms of about 0.011 in  $\mu$ .

wavelength positions of the blend lines. Further, the depth of the core minima (at  $\lambda \approx 4226.6$  Å and  $\lambda \approx 4226.8$  Å) adjacent to the central peak (at  $\lambda_0 = 4226.727$  Å) is significant. The line core is defined as the region between  $\lambda \approx 4226.6$  Å and  $\lambda \approx 4226.8$  Å. The  $Q/I$  in the far wings gradually approaches continuum polarization (see dotted lines in Figure 7(c)).

Although observations are made in the so-called quiet regions, Figure 1 shows pronounced and spatially varying  $U/I$  signals in the line core, which is due to the rotation of the plane of linear polarization by the Hanle effect in the presence of an oriented magnetic field. Some spatial variations in  $(Q/I, U/I)$  along the slit length are seen in the near wings. They were referred to as wing signatures in S09. In this paper, however, we focus only on modeling the average  $Q/I$  spectrum corresponding to the interval 13''–41''. The  $V/I$  signal in Figure 1 is also weak, showing that the longitudinal components of the resolved magnetic field are weak in the observed locations on the solar disk.

#### 3.2. The Smearing Effect

The polarimetric observations for this paper were done with a slit width of 60  $\mu\text{m}$ . To take into account the finite slit width, a convolution of the theoretical  $(I, Q)$  profiles with a slit spectral response function becomes necessary. For simplicity, we assume this function to be a Gaussian. The observed profiles are also broadened by macroturbulent velocity fields. We account for both the broadening effects by using a Gaussian function with a total width at half-maximum of 40 mÅ. The main source of smearing is due to the macroturbulent velocity fields. The smearing due to instrumental broadening is quite small (about 10 mÅ) in comparison.

#### 3.3. The Model Atmosphere and the Model Atom

Figure 2 shows the run of some physical parameters as a function of height in several model atmospheres of the

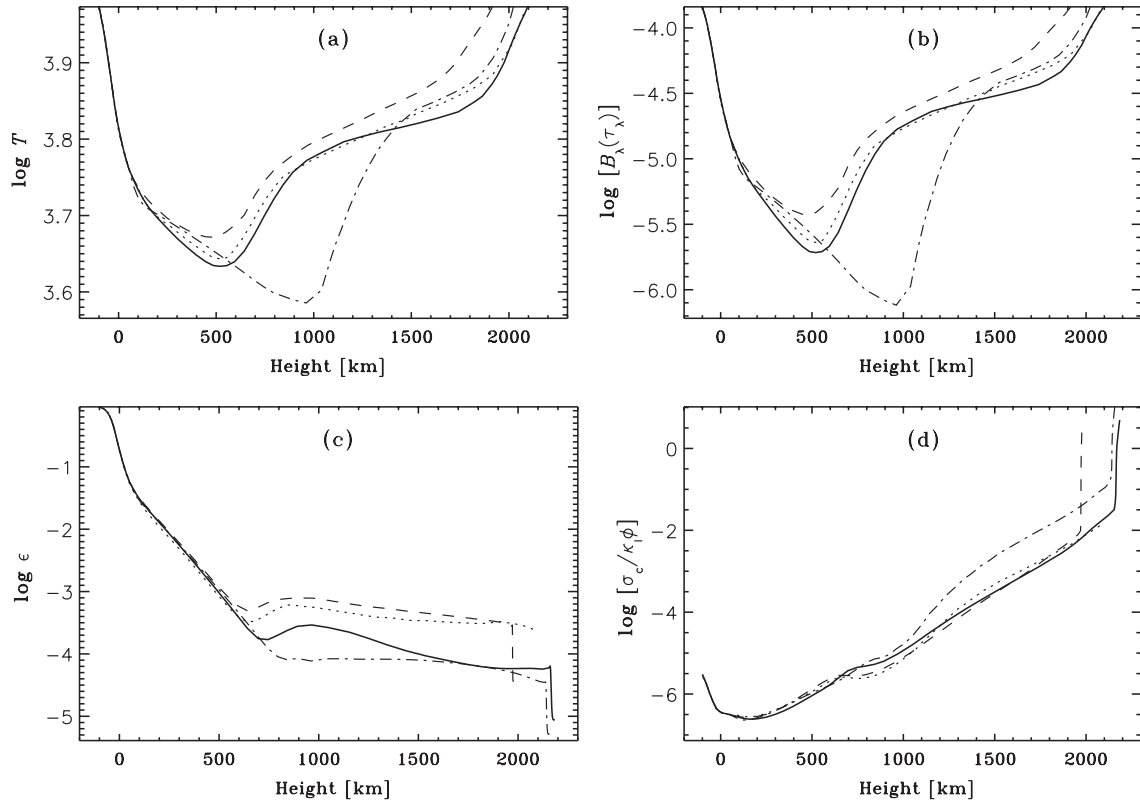


**Figure 2.** Model atmospheres that are tested in this paper in our attempt to fit the observed  $(I, Q/I)$  profiles. Line types: solid, FALA; dotted, FALC; dashed, FALF; dot-dashed, FALX. We find that the FALX model atmosphere provides a reasonable fit to the observations. FALX represents the coolest model, with the chromospheric temperature minimum located around 1000 km above the photosphere (panel a). Panel (b) shows the depth dependence of the Planck function at the line center wavelength. The thermalization parameter  $\epsilon$  remains small and almost constant in the chromospheric layers (panel c). The ratio of the continuum scattering coefficient to the monochromatic line absorption coefficient at the line center reflects the contribution of continuum scattering to the total polarization (panel d). For the FALX model that we use here, the continuum scattering polarization is particularly large in the chromospheric layers, compared to other model atmospheres.

Sun—namely FALA, FALC, FALF (Fontenla et al. 1993), and FALX (Avrett 1995) that we have tested in our attempts to fit the  $(I, Q/I)$  data. The meanings of the abbreviations and the nature of the atmospheric models are described in the given references. Basically, all these models represent the quiet solar atmosphere. For instance, FALA, FALC, and FALF represent, respectively, the super granular cell center, the average quiet Sun, and the bright network region on the solar atmosphere. FALX is a model that was proposed by Avrett (1995) to study the CO molecular observations. We have retained the FALX model for our investigation on the LSAs because it appeared that it could provide a reasonable fit to observations.

In the multilevel RH-code, a Ca I model atom consisting of 20 levels with 17 line transitions and 19 continuum transitions is considered. The main line is treated in PRD. The angle-averaged PRD functions of Hummer (1962) are used for this purpose. All other lines of the multiplet are treated in complete frequency redistribution (CRD). However, for computing the polarization, we restrict ourselves to a two-level atom model for the main line transition. The relevant PRD matrix used for computing  $Q/I$  is given in Equation (A7). All the blend lines are treated in LTE in the RH-code. Therefore, the blend line absorption coefficient is implicitly included in the continuum absorption coefficient  $\kappa_c$ .

#### 4. THE ANISOTROPY FACTOR $k_G(\lambda, \mu, \tau_\lambda)$ AND ITS DEPTH DEPENDENCE IN THE SOLAR MODEL ATMOSPHERE

It is well known that the key factor that determines the shape of the emergent polarization profile is the anisotropy of the

diffuse radiation field within the atmosphere. It is expressed by the parameter  $k_G$ , introduced in Stenflo (1982).  $k_G$  is the factor by which classical scattering polarization is reduced due to angular averaging over the incident radiation, as compared with the case of unidirectional incident radiation. It is given by

$$k_G(\lambda, \mu, \tau_\lambda) = \frac{3}{2\sqrt{2}}(1 - \mu^2)J_0^2(\lambda, \tau_\lambda)/I(\lambda, \mu, \tau_\lambda), \quad (7)$$

with

$$J_0^2(\lambda, \tau_\lambda) = \frac{1}{4\sqrt{2}} \int_{-1}^{+1} d\mu' (3\mu'^2 - 1)I(\lambda, \mu', \tau_\lambda). \quad (8)$$

Here,  $\mu'$  is the direction of the incident radiation field and  $\mu$  is the direction of the scattered beam. The parameter  $k_G$  thus takes care of the actual angular distribution of the radiation field. The integration is over all the incident directions  $\mu'$ . Combining Equations (7) and (8), one recognizes the factor  $(3/8)(1 - \mu^2)(3\mu^2 - 1)$  as the  $(2, 1)$  element of the Rayleigh phase matrix (see the Appendix).

Figure 3 shows the anisotropy factor  $k_G$  for the Ca I 4227 Å line. The dotted lines in both the panels show  $k_G$  computed empirically through a polynomial fit to the observed CLV of intensity  $I$  (see S09). In this way, it represents the observed anisotropy at the surface ( $\tau_\lambda = 0$ ). The other line types in Figure 3(a) correspond to the  $k_G$  calculated using  $I(\lambda, \mu, \tau_\lambda)$  obtained from the RH-code. Throughout this paper, we use the FALX model atmosphere (Avrett 1995). Good agreement

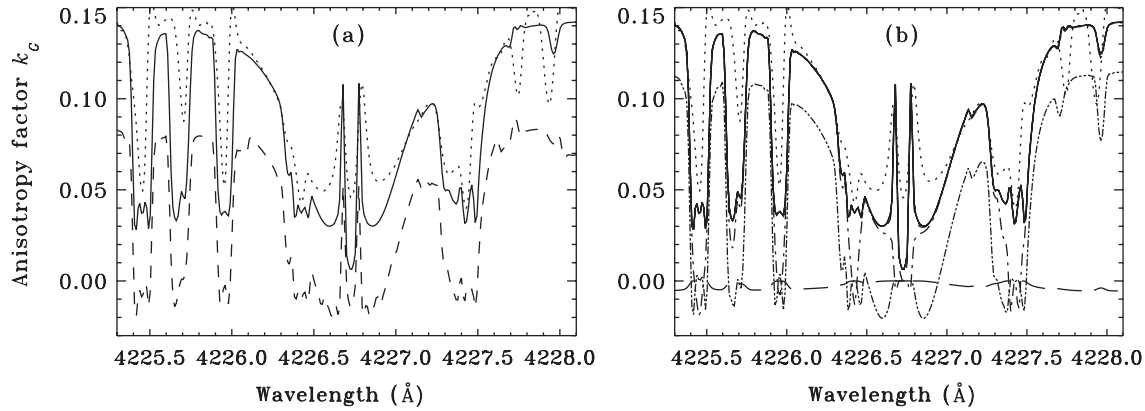


**Figure 3.** Anisotropy factor  $k_G$ . In panel (a), the solid and dashed lines show the theoretically computed  $k_G$  for the FALX model at  $\tau_\lambda = 0$  and  $\tau_\lambda = \mu = 0.1$ , respectively. The dotted lines in both the panels show the  $k_G$  computed from observations (as in S09). In panel (b), we show  $k_G$  at various heights within the solar atmospheric model (FALX). For all heights above the temperature minimum (1000 km),  $k_G$  is shown by the heavy solid line. The other line types are: dot-dashed line = 500 km; dot-dot-dashed line = 200 km; and long-dashed line = -40 km, which correspond to the photospheric layers.

between the theoretically computed  $k_G$  at  $\tau_\lambda = 0$  (solid line) and the observationally derived  $k_G$  (also at  $\tau_\lambda = 0$ ) is a measure of the realism to which the FALX model mimics the solar atmosphere. The dashed line is the  $k_G$  computed at the monochromatic optical depth  $\tau_\lambda = \mu$  for  $\mu = 0.1$ .

Figure 3(b) shows the run of the anisotropy factor  $k_G$  within the solar atmospheric model FALX. The line types correspond to different heights. The long-dashed line represents the deepest layers (-40 km below the photosphere), where the radiation field approaches the Planck function due to thermalization, and therefore  $k_G$  approaches zero. The dot-dashed and dot-dot-dashed lines represent the  $k_G$  in the photospheric layers (500 km and 200 km, respectively). In these layers,  $k_G$  seems to be most sensitive to the optical depth stratification. For all the heights from the temperature minimum at 1000 km and above, the radiation field saturates to nearly a constant value with respect to the depth, and hence the  $k_G$  plots for all these heights merge into a single curve represented by the heavy solid line (in other words,  $k_G$  becomes independent of depth). Holzreuter et al. (2005) have presented a detailed analysis of the correspondence between the depth dependence of the anisotropy and the shape of the emergent  $Q/I$  spectra of this line. A similar argumentation can be used to understand the anisotropy plots presented in Figure 3. Hence we do not elaborate further on this aspect.

## 5. THE LAST SCATTERING APPROXIMATIONS

The concept of LSA implies that one first determines Stokes  $I$ , either through observations or with a numerical calculation in which the polarization is neglected. This is possible for the second solar spectrum because the polarization is a few percent at most. One then assumes that a single scattering of this intensity field suffices to properly evaluate the observed linear polarization. This LSA concept has been used in Stenflo (2005) for the solar continuum polarization, in S09 for the Ca I 4227 Å line, in Belluzzi et al. (2007) for the Ba II D<sub>1</sub> and D<sub>2</sub> lines, and the ratio  $Q/I$  is deduced from the observed Stokes  $I$ . In Faurobert & Arnaud (2002) for the scattering polarization of molecular emission lines, the photospheric intensity field used is a solution of an unpolarized RT equation.

In this paper, we present different levels of approximations based on the concept of LSA. From the most sophisticated one to the most simple one, they are LSA-3, LSA-2, and LSA-1. A common point to these approximations and what makes them

interesting is that they allow one to separately obtain Stokes  $I$  and Stokes  $Q$ . In contrast, in the full RT method,  $I$  and  $Q$  are calculated simultaneously. In LSA-3 and LSA-2, we first calculate Stokes  $I(\lambda, \mu, \tau_\lambda)$  at all the depth points in a solar model atmosphere, ignoring the contribution of Stokes  $Q$  in the source terms  $S_{I,l}$  and  $S_{I,c}$  (see Equations (3) and (4)). In LSA-1 we use the observed intensity (Stokes  $I$ ). To obtain the polarization, we keep only the terms depending on the intensity in the equations for the source terms  $S_{Q,l}$  and  $S_{Q,c}$  (see Equations (3) and (4)). Once  $S_Q$  has been obtained, one can either solve a simple transfer equation to calculate Stokes  $Q$  (this is the LSA-3 approximation) or evaluate Stokes  $Q$  with an Eddington-Barbier relation (this is the LSA-2 approximation). For LSA-1, we use a somewhat different method for the calculation of Stokes  $Q$  (see below).

The approximations LSA-3 and LSA-2 are directly related to the iterative method for calculating linear polarization introduced in Frisch et al. (2009). In this method, as done here, one neglects the polarization for the calculation of Stokes  $I$  but the polarization is kept in the  $Q$  component of the source term and an integral equation is established for this  $S_Q$ . Its solution can be written as a series expansion in the mean number of scattering events. The first term, which gives the value of  $S_Q$  after a single scattering of the incident radiation field depends only on Stokes  $I$  and is identical to our approximation. The following terms in the expansion take into account additional scattering events. They can be calculated iteratively.

We now describe in detail the LSA-3, LSA-2, and LSA-1 approximations.

### 5.1. LSA-3

As explained in Section 5, we neglect the contribution of  $Q(\lambda, \mu, \tau_\lambda)$  on the right-hand side of the equations for  $S_{I,l}(\lambda, \mu, \tau_\lambda)$  and  $S_{Q,l}(\lambda, \mu, \tau_\lambda)$ . Therefore, Equation (3) can be written as

$$[S_{I,l}(\lambda, \mu, \tau_\lambda)]_{\text{LSA-3}} = \frac{1 - \epsilon}{\phi(\lambda, z)} \int_{-1}^{+1} \frac{d\mu'}{2} \int_0^\infty d\lambda' \times R_{11}(\lambda, \lambda', \mu, \mu', z) I(\lambda', \mu', \tau_{\lambda'}) + \epsilon B_\lambda(\tau_\lambda) \quad (9)$$

for  $S_{I,l}$ , and

$$[S_{Q,l}(\lambda, \mu, \tau_\lambda)]_{\text{LSA-3}} = \frac{1 - \epsilon}{\phi(\lambda, z)} \int_{-1}^{+1} \frac{d\mu'}{2} \int_0^\infty d\lambda' \times R_{21}(\lambda, \lambda', \mu, \mu', z) I(\lambda', \mu', \tau_{\lambda'}) \quad (10)$$

for  $S_{Q,I}$ . Here,  $\tau_\lambda$  and  $\tau_{\lambda'}$  stand for  $\tau_\lambda(z)$  and  $\tau_{\lambda'}(z)$ , respectively. This also holds for Equations (15), (17), (23), and (24) below.

### 5.1.1. LSA-3 with Angle-averaged Partial Redistribution

In this section, we restrict our attention to the use of the angle-averaged version of the Domke–Hubeny redistribution matrix (see Equation (A7)). For this particular choice, the redistribution matrix elements can be written as

$$R_{11}(\lambda, \lambda', \mu, \mu', z) = R^{(0)}(\lambda, \lambda', z) + R^{(2)}(\lambda, \lambda', z)P_{11}^{(2)}(\mu, \mu') \quad (11)$$

and

$$R_{21}(\lambda, \lambda', \mu, \mu', z) = R^{(2)}(\lambda, \lambda', z)P_{21}^{(2)}(\mu, \mu'), \quad (12)$$

where

$$R^{(0)}(\lambda, \lambda', z) = \gamma_{\text{coh}}R_{\text{II}}(\lambda, \lambda', z) + (1 - \gamma_{\text{coh}})R_{\text{III}}(\lambda, \lambda', z), \quad (13)$$

$$R^{(2)}(\lambda, \lambda', z) = W_2[\gamma_{\text{coh}}R_{\text{II}}(\lambda, \lambda', z) + (1 - \gamma_{\text{coh}})k_c R_{\text{III}}(\lambda, \lambda', z)]. \quad (14)$$

Substituting Equation (11) into Equation (9), we obtain

$$[S_{I,I}(\lambda, \tau_\lambda)]_{\text{LSA-3}} = \epsilon B_\lambda(\tau_\lambda) + \frac{1 - \epsilon}{\phi(\lambda, z)} \int_0^\infty d\lambda' R^{(0)}(\lambda, \lambda', z) J(\lambda', \tau_{\lambda'}), \quad (15)$$

where

$$J(\lambda', \tau_{\lambda'}) = \int_{-1}^{+1} \frac{d\mu'}{2} I(\lambda', \mu', \tau_{\lambda'}). \quad (16)$$

In Equation (15), the contribution from  $R^{(2)}P_{11}^{(2)}$  is neglected because it is on the order of polarization and hence much smaller than the contribution from the term  $R^{(0)}J$ . Substituting Equation (12) into Equation (10), we get

$$[S_{Q,I}(\lambda, \mu, \tau_\lambda)]_{\text{LSA-3}} = \frac{3}{2\sqrt{2}} \frac{1 - \epsilon}{\phi(\lambda, z)} (1 - \mu^2) \times \int_0^\infty d\lambda' R^{(2)}(\lambda, \lambda', z) J_0^2(\lambda', \tau_{\lambda'}), \quad (17)$$

where  $J_0^2(\lambda', \tau_{\lambda'})$  is defined in Equation (8).

So far we considered only the line source functions. Clearly, the continuum is also polarized and needs to be appropriately included. The LSA concept can again be applied to obtain a simpler expression for  $S_{I,c}$  and  $S_{Q,c}$ , namely

$$[S_{I,c}(\lambda, \tau_\lambda)]_{\text{LSA-3}} = J(\lambda, \tau_\lambda) \quad (18)$$

and

$$[S_{Q,c}(\lambda, \mu, \tau_\lambda)]_{\text{LSA-3}} = \frac{3}{2\sqrt{2}} (1 - \mu^2) J_0^2(\lambda, \tau_\lambda). \quad (19)$$

The total source functions  $[S_I(\lambda, \tau_\lambda)]_{\text{LSA-3}}$  and  $[S_Q(\lambda, \mu, \tau_\lambda)]_{\text{LSA-3}}$  can be computed by substituting Equations (15), (17),

(18), and (19) into Equation (2). Finally, we obtain an approximate formula for the emergent  $Q/I$  by using  $S_I$  and  $S_Q$  computed above in the formal solution expression (Equation (5)), namely

$$\left[ \frac{Q}{I}(\lambda, \mu) \right]_{\text{LSA-3}} = s \int_0^{\tau_\lambda} \frac{d\tau'_\lambda}{\mu} \exp\left(-\frac{\tau'_\lambda}{\mu}\right) \times [S_Q(\lambda, \mu, \tau'_\lambda)]_{\text{LSA-3}} / \int_0^{\tau_\lambda} \frac{d\tau'_\lambda}{\mu} \exp\left(-\frac{\tau'_\lambda}{\mu}\right) \times [S_I(\lambda, \tau'_\lambda)]_{\text{LSA-3}}. \quad (20)$$

In the denominator of the above equation, we have neglected the contribution from incident intensity at the lower boundary. The quantity  $s$  is a global scaling parameter. It is a free parameter that is used to achieve a fit of the  $Q/I$  computed by the LSA approach with the  $Q/I$  computed from the RT benchmark. Ideally it should be unity. But in practice it can take values either smaller or slightly larger than unity. It can therefore be used as a measure of the goodness of the last scattering approximations (see Section 6.2.1).

In the RT approach, we compute polarization by perturbation. First, we give the initial unpolarized source vector as input and calculate the Stokes vector using a formal solution. A new source vector is then computed using the improved Stokes vector—and this process is repeated. In LSA-3, we avoid this perturbative loop. For the calculation of Stokes  $I$ , we ignore the polarization. The component  $S_Q$  of the source function is deduced from the explicit expressions given in Equations (17) and (19) which involve only integrations over the directions and frequencies of Stokes  $I$ . Stokes  $Q$  can then be calculated by using a formal solver.

### 5.1.2. LSA-3 with Angle-dependent Partial Redistribution

In this section, we present a formula for  $Q/I$  that can be used in the case of the angle-dependent ( $\mu$ -dependent, but azimuthally averaged) redistribution matrices given in Equation (A6). In this case, the redistribution matrix elements can be written as

$$R_{11}(\lambda, \lambda', \mu, \mu', z) = R^{(0)}(\lambda, \lambda', \mu, \mu', z) + R^{(2)}(\lambda, \lambda', \mu, \mu', z)P_{11}^{(2)}(\mu, \mu') \quad (21)$$

and

$$R_{21}(\lambda, \lambda', \mu, \mu', z) = R^{(2)}(\lambda, \lambda', \mu, \mu', z)P_{21}^{(2)}(\mu, \mu'). \quad (22)$$

Here,  $R^{(0)}(\lambda, \lambda', \mu, \mu', z)$  and  $R^{(2)}(\lambda, \lambda', \mu, \mu', z)$  have the same form as the functions  $R^{(0)}(\lambda, \lambda', z)$  and  $R^{(2)}(\lambda, \lambda', z)$  given in Equations (13) and (14), but with the replacements  $R_{\text{II,III}}(\lambda, \lambda', z) \rightarrow R_{\text{II,III}}(\lambda, \lambda', \mu, \mu', z)$ . We recall that angle-dependent partial redistribution (in the presence of a magnetic field) was used in S09. A simple formula for  $Q/I$  was given in S09 by assuming  $\mu' = 1$  in the expression for the redistribution matrix elements. We can apply the same approximation to the redistribution functions  $R^{(0)}(\lambda, \lambda', \mu, \mu', z)$  and  $R^{(2)}(\lambda, \lambda', \mu, \mu', z)$ . With this approximation, we now obtain

$$[S_{I,I}(\lambda, \mu, \tau_\lambda)]_{\text{LSA-3}}^{\text{AD}} = \epsilon B_\lambda(\tau_\lambda) + \frac{1 - \epsilon}{\phi(\lambda, z)} \int_0^\infty d\lambda' \times R^{(0)}(\lambda, \lambda', \mu, \mu' = 1, z) J(\lambda', \tau_{\lambda'}) \quad (23)$$

and

$$\begin{aligned} & [S_{Q,I}(\lambda, \mu, \tau_\lambda)]_{\text{LSA-3}}^{\text{AD}} \\ &= \frac{1 - \epsilon}{\phi(\lambda, z)} \frac{3}{2\sqrt{2}} (1 - \mu^2) \\ & \times \int_0^\infty d\lambda' R^{(2)}(\lambda, \lambda', \mu, \mu' = 1, z) J_0^2(\lambda', \tau_{\lambda'}). \quad (24) \end{aligned}$$

The symbol AD refers to the case of angle-dependent partial redistribution. The above equations along with Equations (18) and (19) can be used to compute the total source functions  $S_I$  and  $S_Q$ . The  $Q/I$  can be calculated from Equation (20) using these  $S_I$  and  $S_Q$ .

### 5.2. LSA-2: Eddington–Barbier Approximation

We proceed exactly as with LSA-3 but use the Eddington–Barbier approximation to calculate  $Q$  and  $I$  once  $S_Q$  and  $S_I$  have been determined. We also set the thermalization parameter  $\epsilon = 0$ . Equation (20) is replaced by

$$\left[ \frac{Q}{I}(\lambda, \mu) \right]_{\text{LSA-2}} = s \frac{S_Q(\lambda, \mu, \tau_\lambda(z_{\lambda,\mu}))}{S_I(\lambda, \tau_\lambda(z_{\lambda,\mu}))}, \quad (25)$$

where  $z_{\lambda,\mu}$  denotes the point in space where  $\tau_\lambda = \mu$ , for a given  $\lambda$  and a given  $\mu$ . Equation (25) is the polarized analog of the Eddington–Barbier relation for Stokes  $I$  (see Mihalas 1978, p. 39). The Eddington–Barbier approximation for  $Q/I$  has been shown by several authors to be useful. See, e.g., Faurobert (1987, 1988) who used it for a semi-quantitative analysis of the linear polarization profiles formed in an isothermal atmosphere.

### 5.3. LSA-1: Semi-empirical Approach

In LSA-1, we use the observed CLV of Stokes  $I$  to calculate the anisotropy factor  $k_G$  and, as done in S09, assume that the ratio  $Q/I$  may be written as

$$\begin{aligned} & \left[ \frac{Q}{I}(\lambda, \mu) \right]_{\text{LSA-1}} = s \left[ \frac{\phi(\lambda)}{\phi(\lambda) + C} \right. \\ & \left. \times [Z_{Q,I}(\lambda, \mu, 0)]_{\text{LSA-1}} + \frac{C}{\phi(\lambda) + C} P_C \right], \quad (26) \end{aligned}$$

with

$$\begin{aligned} & [Z_{Q,I}(\lambda, \mu, 0)]_{\text{LSA-1}} \\ &= \frac{3}{2\sqrt{2}} (1 - \mu^2) \frac{\int_0^\infty d\lambda' R^{(2)}(\lambda, \lambda') J_0^2(\lambda', 0)}{\int_0^\infty d\lambda' R^{(0)}(\lambda, \lambda') I(\lambda', \mu, 0)}, \quad (27) \end{aligned}$$

where  $R^{(2)}$  and  $R^{(0)}$  are taken to be independent of depth and are computed for a damping parameter corresponding to a chosen value of  $\Gamma_E/\Gamma_R$  and  $\Gamma_I/\Gamma_R$  set to zero. As in S09,  $\Gamma_E/\Gamma_R$  is treated as a free parameter. In Equation (26),  $C$  is the ratio of continuum to the line-averaged opacity and  $P_C$  is the continuum polarization. Here,  $s$ ,  $C$ , and  $P_C$  are treated as free parameters

for a chosen value of  $\Gamma_E/\Gamma_R$ . We refer to S09 for details on the use of LSA-1 to model the Ca I 4227 Å line wings in the  $Q/I$  spectra.

## 6. RESULTS AND DISCUSSIONS

In this section, we first show how well the approximate solutions introduced above compare with the RT solution. Subsequently, we also demonstrate how the formulas for  $Q/I$  derived under different levels of the LSA approach can be used in a preliminary analysis of the observed  $Q/I$  spectra.

### 6.1. Theoretical Validation of the LSA Approaches

In this section, we use the RT solution as a theoretical benchmark. In Figure 4, we compare LSA-3 solutions with the benchmark RT solution for different values of  $\mu$ . Figure 4 shows that the agreement between the LSA-3 approximation and the full RT calculation is excellent, except for the central peak and wing minima. We stress that in this figure the scaling factor is  $s = 1$ . The differences in the line core region are due to the fact that we have neglected the contribution of  $Q$  in the expression of  $S_{Q,I}$ . This contribution plays a significant role in the line core (Frisch et al. 2009). Figure 4 also shows that the LSA-3 approach is valid for any value of  $\mu$ .

Figure 5 shows a comparison of  $Q/I$  computed by the RT approach (dot-dot-dashed lines) and different levels of the LSA approach (solid lines) for  $\mu = 0.1$ . Panel (a) of Figure 5 is identical to panel (a) of Figure 4. As the LSA-3 approximation has already been discussed above, we concentrate now on LSA-2 and LSA-1. Figure 5(b) shows that LSA-2, which makes use of the Eddington–Barbier relation, can fit the line wings, including the near wing maxima, rather well provided one applies a scaling factor of  $s = 1.6$ . Here we note that we obtain essentially the same  $Q/I$  profile if the Eddington–Barbier approximation is used for the calculation of  $Q$  only.

In the line core, LSA-2 is clearly not an acceptable approximation. We recall that the Eddington–Barbier approximation, which amounts to replacing an integral of the form  $I(\mu) = \int_0^\infty S(\tau) e^{-\tau/\mu} (d\tau/\mu)$  by  $I(\mu) = S(\mu)$ , provides an exact value of  $I(\mu)$  when  $S$  is a linear function of  $\tau$ . So the accuracy of this approximation will depend on the departures of  $S(\tau)$  from linearity. For the line Ca I 4227 Å,  $S_Q(\lambda, \mu, \tau_\lambda)$  has a non-monotonic variation when  $\lambda$  is around the line center. So the failure of the Eddington–Barbier approximation in this wavelength range is not surprising. In the line wings  $S_Q(\lambda, \mu, \tau_\lambda)$  increases regularly toward the surface, following the increase in the anisotropy of the radiation field (see Figure 3(a)) but the increase is much faster than linear. Therefore, the Eddington–Barbier approximation underestimates the value of  $Q$  and a scaling factor of  $s = 1.6$  is needed to fit the RT calculation. A comparison between panels (a) and (b) in Figure 5 clearly shows that the depth dependence of the anisotropy factor  $k_G$  has to be taken into account for a proper modeling of the line center peak. For strong chromospheric lines such as Ca I 4227 Å, an accurate non-LTE treatment of the line formation is needed to calculate this depth dependence with accuracy.

Figure 5(c) shows that LSA-1 can be made to fit the top envelopes of the PRD peaks of the Ca I 4227 Å line, blend lines, and the far wing continuum polarization, with a proper choice of the free parameters as it does in S09. The free parameters used in Figure 5(c) to compare the LSA-1 and RT solution are:  $s = 0.9$ ,  $C = 2.1 \times 10^{-3}$ , and  $P_C = 0.0013$ , for a

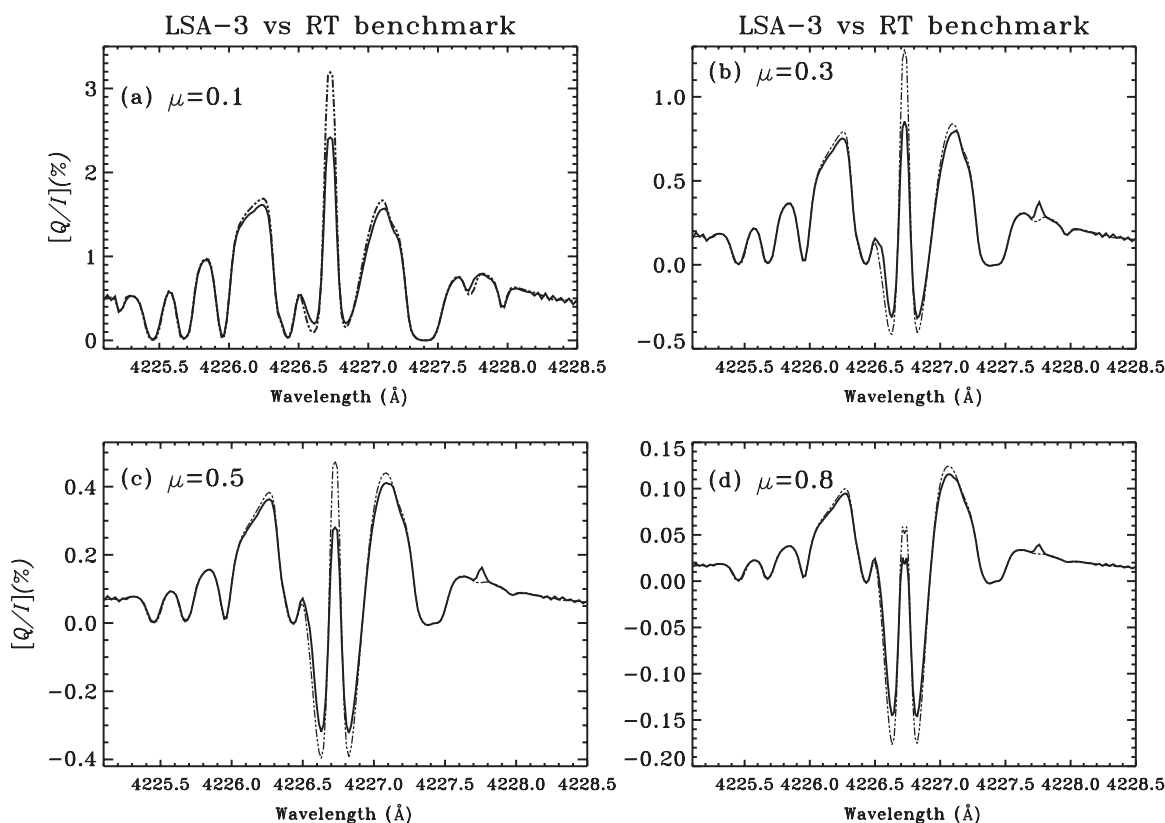


Figure 4. Comparison of  $Q/I$  computed by the LSA-3 approach (solid lines) with the benchmark solution computed by the RT approach (dot-dot-dashed lines), for different values of  $\mu$ . The global scaling parameter  $s$  for the LSA-3 is unity for all the panels.

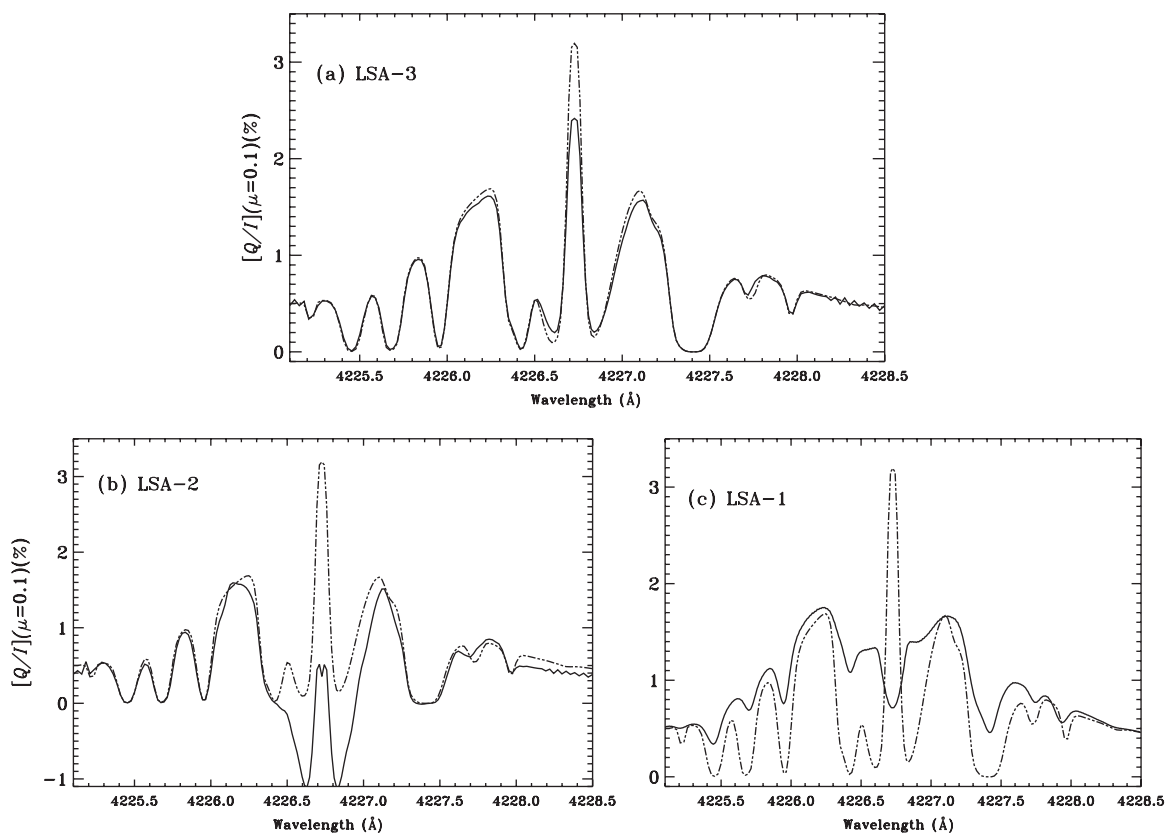
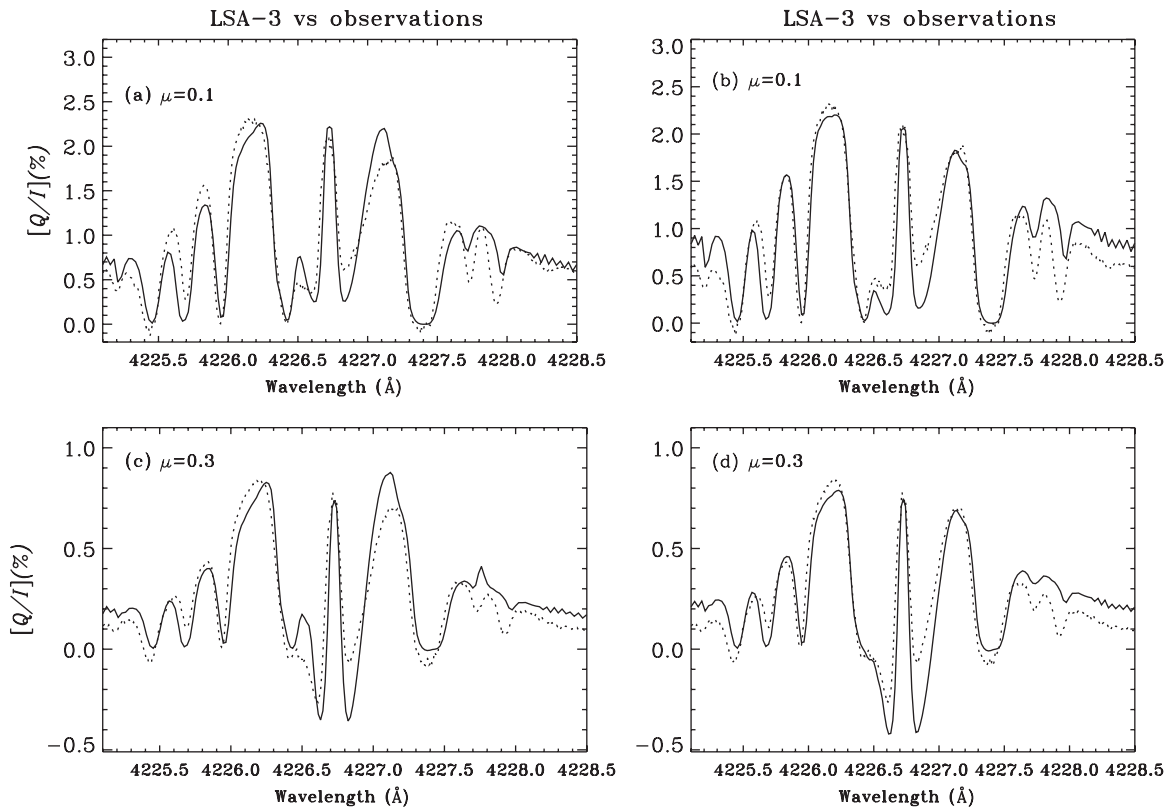


Figure 5. Comparison of  $Q/I$  for different LSA approaches (solid lines) and the solution computed by the RT approach (dot-dot-dashed lines). Note that different levels of LSA require different extents of the global scaling parameter  $s$  ( $= 1, 1.6,$  and  $0.9,$  respectively, for LSA-3, LSA-2, and LSA-1).



**Figure 6.** Comparison of  $Q/I$  computed by the LSA-3 approach (solid lines) and the observations taken during 2010 January (dotted lines). The scaling parameter  $s_{\text{obs}} = 1.4, 1.8, 1.1,$  and  $1.35,$  respectively, for panels (a), (b), (c), and (d). Panels (b) and (d) are based on an increase of the elastic collision rate  $\Gamma_{E,vW}$  by a factor of 1.5, which improves the fit significantly. The fit of the core peak is optimized by using a microturbulent magnetic field of strength 15, 25, 10, and 15 G for panels (a)–(d).

chosen  $\Gamma_E/\Gamma_R = 10$ . We recall that LSA-1 requires no numerical solution of transfer equations and is independent of the model atmosphere.

## 6.2. Observational Validation of the LSA-3 and RT Approaches

In Figures 6 and 7, we compare the observations with predictions from the LSA-3 and RT calculations for  $\mu = 0.1$  and  $\mu = 0.3$ . Figure 6 shows  $Q/I$  computed by the LSA-3 approximation. Figure 7 shows the  $Q/I$  profiles and also the intensity profile from the RT approach.  $I$  is actually computed using the polarized RT approach. However, this  $I$  does not differ very much from the intensity computed by the unpolarized RH-code.

Three free parameters are used in the modeling procedure. They are (1) an enhancement parameter  $c$ , associated with the elastic collision rate  $\Gamma_{E,vW}$  (of the van der Waal type), (2) a global scaling parameter  $s_{\text{obs}}$ , and (3) a microturbulent magnetic field  $B_{\text{turb}}$ .

With an appropriate choice of these three free parameters, we can achieve a reasonable fit of the theoretical  $Q/I$  profile with observations for all the wavelengths. We first choose a value of  $c$  not far from unity (here we have chosen  $c = 1$  and  $c = 1.5$ ), then determine  $s_{\text{obs}}$  by a fit to the wings and finally  $B_{\text{turb}}$  by a fit of the core peak. The choice of  $s_{\text{obs}}$  is done by requiring an overall simultaneous fit to the PRD peaks and the blend line minima over all of the  $Q/I$  wings. The values of the three free parameters used in Figures 6 and 7 are listed in Table 1.

**Table 1**

Values of Free Parameters Used in Modeling the Observed  $Q/I$  Spectra

Approach	Figure	$\mu$	$c$	$s_{\text{obs}}$	$B_{\text{turb}}$
LSA-3	6(a)	0.1	1	1.4	15
RT	7(c)	0.1	1	1.4	20
LSA-3	6(b)	0.1	1.5	1.8	25
RT	7(c)	0.1	1.5	1.8	30
LSA-3	6(c)	0.3	1	1.1	10
RT	7(d)	0.3	1	1.1	15
LSA-3	6(d)	0.3	1.5	1.35	15
RT	7(d)	0.3	1.5	1.35	20

### 6.2.1. The Role of Global Scaling Parameter $s_{\text{obs}}$ in Modeling the $Q/I$ Profile

To compare the theoretical  $Q/I$  with the observed  $Q/I$  profile as the new benchmark, we introduce a new scaling parameter denoted by  $s_{\text{obs}}$ , which multiplies both the LSA-3 and RT profiles.  $s_{\text{obs}}$  is different from  $s$ , which was used as the scaling parameter when the RT solution was the benchmark (see Figures 4 and 5). It is defined as

$$s_{\text{obs}} = \frac{[(Q/I)_{\text{wing}}]_{\text{observed}}}{[(Q/I)_{\text{wing}}]_{\text{theory}}}. \quad (28)$$

While one might expect that  $s_{\text{obs}}$  should be close to unity, Figures 6(a) and (c) require  $s_{\text{obs}} = 1.4$  and  $1.1$ , respectively. Figures 6(b) and (d) need even larger values of  $s_{\text{obs}}$ , namely 1.8 and 1.35, respectively. Such increased values of  $s_{\text{obs}}$  become necessary to account for the depolarization caused by the

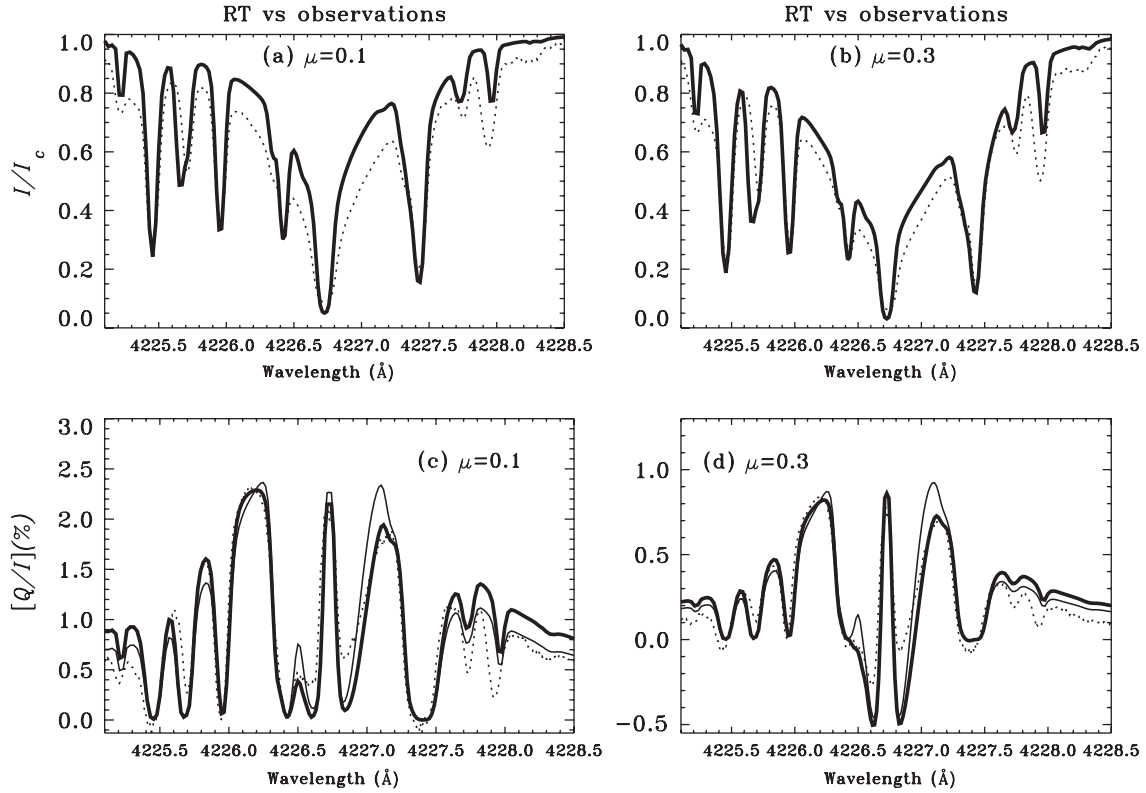


**Figure 7.** Comparison of  $(I, Q/I)$  spectra computed using the RT approach (solid lines) and the observations taken during 2010 January (dotted lines). Thick solid lines correspond to the case of  $\Gamma_{E,vW}$  enhanced by a factor of 1.5 (the line that matches with the observed data closely at the PRD peaks). Thin solid lines are without any such enhancement of  $\Gamma_{E,vW}$ . In panel (c), we require  $s_{\text{obs}} = 1.4$  (for thin solid line) and 1.8 (for thick solid line). In panel (d), we require  $s_{\text{obs}} = 1.1$  (for thin solid line) and 1.35 (for thick solid line). In panel (c), thin and thick solid lines correspond to  $B_{\text{turb}} = 20$  G and 30 G, respectively. Similarly,  $B_{\text{turb}} = 15$  G and 20 G for the thin and thick solid lines in panel (d). The continuum intensity  $I_c$  is chosen at  $\lambda = 4228.8$  Å.

enhancement of  $\Gamma_{E,vW}$  (the necessity for an enhancement of the elastic collision rates in our model fitting is discussed in Section 6.2.2). The values of  $s_{\text{obs}}$  needed for the LSA-3 and RT approaches are the same (see Figures 7(c) and (d); Table 1). Note that for  $\mu = 0.3$  the value of  $s_{\text{obs}}$  is closer to unity than it is for  $\mu = 0.1$ .

The rationale behind the use of the scaling parameters can be explained as follows: when comparing two  $Q/I$  spectra, either LSA with RT (for which the scaling factor  $s$  is introduced) or LSA and RT with observations (for which the scaling factor  $s_{\text{obs}}$  is introduced), there are two aspects of the comparison: (a) the relative shapes of the  $Q/I$  spectra and (b) the absolute  $Q/I$  amplitudes. Aspect (a) is much more important than aspect (b) for various reasons. (1) The relative shapes between observations and theory (RT and LSA) can be brought to good agreement, in contrast to the absolute amplitudes. (2) For magnetic field determinations, one should not use the absolute  $Q/I$  core amplitude, but instead the ratio between the core and wing amplitudes (see Section 6.2.3). With this differential approach any global scale error divides out, greatly reducing the effects of model deficiencies. (3) The absolute  $Q/I$  amplitudes are, in addition to the model deficiencies, directly affected by observational errors in the  $\mu$  value. These observational errors divide out with the differential approach.

The parameter  $s_{\text{obs}}$  is essential for a comparison of the relative shapes of the theoretical  $Q/I$  profiles with the observed ones when  $s_{\text{obs}}$  differs from unity. The circumstance that  $s_{\text{obs}}$  for both RT and LSA-3 differs significantly from unity is an indicator of deficiencies in the modeling of this particular line. Another indicator that there is indeed a modeling problem is the relatively poor fit of the theoretical Stokes  $I$  profiles with the observed

Stokes  $I$ . The discrepancies are particularly large for  $\mu = 0.1$ . Possible causes for  $s_{\text{obs}}$  to deviate from unity are (1) the choice of model atmosphere, (2) the use of one-dimensional geometry to represent the solar atmosphere, (3) the use of angle-averaged redistribution functions, and (4) observational uncertainties in the value of  $\mu$ .

The parameter  $s_{\text{obs}}$  absorbs all these as well as possible unknown sources of errors. In addition, the degree of deviation of the scaling factors  $s$  and  $s_{\text{obs}}$  from unity can be used as a measure of the goodness of the model fit.

### 6.2.2. The Role of Elastic Collision Rate $\Gamma_{E,vW}$ in Modeling the $Q/I$ Wings

We have found that in fitting the  $Q/I$  wing shape, an enhanced value of  $\Gamma_{E,vW}$  becomes necessary. We denote this enhancement parameter by  $c$ . It is used as a source of additional broadening. In Figures 6(a) and (c), we have set  $c = 1$ . In Figures 6(b) and (d), we have used  $c = 1.5$ . One can notice a substantial improvement in fitting the shape of the  $Q/I$  profile, when going from  $c = 1$  to  $c = 1.5$ , in particular in reproducing the asymmetry of the wing maxima. Similar enhancement was also applied by Faurobert-Scholl (1992) to fit the observed  $Q/I$  wing polarization. The justification for this can be found in Derouich et al. (2003) and Barklem & O'Mara (1997) who, respectively, show that the old theories of  $D^{(2)}$  and elastic collision rate  $\Gamma_E$  actually underestimate  $\Gamma_{E,vW}$ . An enhanced value of  $\Gamma_{E,vW}$  causes depolarization (decrease of  $Q/I$  in magnitude) in the line wings which are formed in the deeper layers of the atmosphere where collision rates are higher. This wing depolarization can be compensated for by using an appropriate value of  $s_{\text{obs}}$  to obtain the actual magnitude of  $Q/I$  in the wings.

In Figures 7(c) and (d), we show a comparison of the  $Q/I$  computed by the RT approach and the observations. In these two panels, one can also notice the improvement in fitting the shape of the  $Q/I$  wings when  $c = 1.5$  (thick solid lines), as compared to the case of  $c = 1$  (thin solid lines).

### 6.2.3. The Role of Microturbulent Magnetic Field $B_{\text{turb}}$ in Modeling the $Q/I$ Core Peak

Once a reasonable fit to the  $Q/I$  wings is achieved, we focus on obtaining a good fit to the  $Q/I$  at the line core. This can be done by using an appropriate value of  $B_{\text{turb}}$  which is the third free parameter.

In other words,  $B_{\text{turb}}$  can be determined by demanding that

$$\frac{[(Q/I)_{\text{core}}]_{\text{observed}}}{[(Q/I)_{\text{wing}}]_{\text{observed}}} = \frac{[(Q/I)_{\text{core}}]_{\text{theory}, B_{\text{turb}} \neq 0}}{[(Q/I)_{\text{wing}}]_{\text{theory}}} \quad (29)$$

should be satisfied. We can rewrite Equation (29) as

$$[(Q/I)_{\text{core}}]_{\text{observed}} = s_{\text{obs}} [(Q/I)_{\text{core}}]_{\text{theory}, B_{\text{turb}} \neq 0}, \quad (30)$$

where  $s_{\text{obs}}$  is defined in Equation (28). In Equation (29),  $[(Q/I)_{\text{core}}]_{\text{theory}, B_{\text{turb}} \neq 0}$  is obtained either from LSA-3 or from the RT approach. It depends on  $f_B$  (which is a function of  $B_{\text{turb}}$ ) defined in Equation (A11) through the modified phase matrix elements. The value of  $B_{\text{turb}}$  is found by solving Equation (30). The described procedure is a differential approach for determining  $B_{\text{turb}}$  because we use the ratio of the core peak to the wing peak amplitudes, instead of the absolute core peak amplitudes.

The set of values of  $B_{\text{turb}}$  deduced from the LSA-3 approach is systematically smaller than that deduced from the RT approach (see Table 1). This is essentially due to the underestimation of the core peak values by LSA-3 (see Figures 4 and 5(a)). This underestimation of  $B_{\text{turb}}$  when using LSA-3 instead of a full RT calculation is not specific to the Ca I 4227 Å line. It will appear whenever one uses an LSA-3 approximation rather than a full RT approach to evaluate the linear polarization of the strong resonance lines.

## 7. CONCLUSIONS

In this paper, we develop a mathematical framework for the LSA approach, starting from the polarized RT equation. We derive simple formulas for  $Q/I$  by applying a few approximations to the governing equations of the RT approach.

LSA-1 is the simplest approach, which is based on observationally derived anisotropy at the surface (it was used in S09 to explore the wing signatures observed in the Ca I 4227 Å line). It ignores the depth variation of all the physical quantities. For this reason, LSA-1 fits only qualitatively the PRD peaks and the envelopes of the wings in the  $Q/I$  spectra. The line core itself as well as the core minima could not be reproduced using LSA-1. In this paper, we aim at modeling various features (including the line core) of the observed  $Q/I$  spectra of this line in a greater detail. To this end, we generalize the LSA-1 by introducing two more levels of LSA, namely LSA-2 and LSA-3. We find that the LSA-2 approach, which takes into account the anisotropy factor at atmospheric heights where the condition  $\tau_\lambda = \mu$  (for a given  $\mu$  and a given  $\lambda$ ) is satisfied, is insufficient to reproduce the line core region. The only way to adequately model the core region without using the full polarized RT approach is through LSA-3. This is because, unlike LSA-1 and LSA-2, LSA-3 takes into account the run of the anisotropy factor over

the optical depth, apart from taking the depth dependence of other concerned physical quantities.

We validate the LSA approaches by comparing it with the RT approach. The advantage of the LSA-3 (and also the LSA-2) approach is that it is sufficient to solve the unpolarized RT equation only once to obtain accurate values of  $I(\lambda, \mu, \tau_\lambda)$ , opacities, and collision rates throughout the atmosphere. These are subsequently used as inputs to the approximate LSA formulas to evaluate the emergent  $Q/I$  spectra. In this way, we avoid solving the polarized RT equation—which is computationally more expensive. As for the timing efficiency, LSA-1 is 21 times faster than LSA-2, 25 times faster than LSA-3, and 58 times faster than the RT approach. The main advantage of LSA-1 is that it does not need the solution from the RH-code (on the other hand, the inputs from the RH-code are needed by LSA-2, LSA-3, and also the polarized RT). In the relative comparison between LSA-2, LSA-3, and the RT approaches, the time taken by the RH-code to compute Stokes  $I$  is excluded, because it is common to all of them. Thus, LSA-2 is 5 times faster than LSA-3 and 38 times faster than RT approach. LSA-3 is 8 times faster than the RT approach. Therefore, compared with the full scale polarized RT approach, the LSA approaches are quite efficient.

To illustrate the usefulness of the LSA-3 approach in modeling the second solar spectrum, we compare both the LSA-3 and the RT solutions with the recently observed  $Q/I$  spectra of the Ca I 4227 Å line. These recent observations are made in the quiet regions on the Sun. In modeling efforts both the LSA-3 and the RT approaches require three free parameters, namely an enhancement parameter  $c$ , associated with the elastic collision rate  $\Gamma_{E,vW}$ , a global scaling parameter  $s_{\text{obs}}$  that accounts for all the known and unknown sources of errors, and a microturbulent magnetic field strength  $B_{\text{turb}}$ .

LSA-1 can only be useful for certain qualitative studies of wing effects, e.g., to explore the existence of the wing Hanle effect (see S09), or to study quantum interference in the Ca II H and K lines (see Stenflo 1980). Although LSA-2 can be used to perform wing analysis in the same way as LSA-1, computationally it is not as advantageous as LSA-1. As for LSA-3, it gives a reasonable fit to the observed  $Q/I$  throughout the line profile (including the line core). Thus, the main advancement of this paper compared to S09 is that we have improved the fit to the important features of the observed  $Q/I$  spectra such as (1) core peak, (2) asymmetric core minima, (3) asymmetric PRD peaks in the near wings, (4) blend line polarization, and (5) far wing polarization.

In this paper, we have shown that LSA-3 can provide a fit to the observed  $Q/I$  spectra, which is nearly as good as the RT approach itself. As mentioned above, this can be achieved at a lower computational cost. Thus, LSA-3 may be applied (1) to interpret the second solar spectrum and the Hanle effect in lines with PRD, (2) to test different theories of the elastic collisions, (3) to explore the formation of the second solar spectrum in media where three-dimensional RT effects have to be taken into account, and (4) to estimate the strength of microturbulent magnetic fields in the solar chromosphere.

The authors are grateful to Dr. Dominique Fluri who kindly supplied the code that is used to compute the RT results presented in this paper. K.N.N. and L.S.A. thank Dr. Han Uitenbroek for useful discussions, and for providing a version of his RH-code. K.N.N. and L.S.A. thank ISJRP, the Indo-Swiss Joint Research Program (founded in 2004 by the Swiss State Secretariat of Education and Research-SER and the Indian

Department of Science and Technology-DST), and IRSOL for supporting their visit in 2009. IRSOL is financed by Canton Ticino, ETHZ, and the City of Locarno together with the municipalities affiliated with CISL. The project was supported by the Swiss National Science Foundation (SNSF) grant 200020-117821.

## APPENDIX

### THE REDISTRIBUTION MATRICES

We are primarily interested in a one-dimensional polarized RT problem. In this appendix, we briefly discuss the polarized redistribution matrices in the Stokes  $(I, Q, U)$  basis. The use of  $(I, Q, U)$  becomes necessary whenever there is non-axisymmetry in the problem, the two well-known examples of which are (1) the incidence of non-axisymmetric radiation at the boundary and (2) the presence of an oriented magnetic field. Both of these break the azimuthal symmetry of the radiation field. In axisymmetric problems, we can work with the  $(I, Q)$  basis, as  $U \equiv 0$ . In this paper,  $Q$  positive is defined to be parallel to the limb. We begin by writing down the redistribution matrix for non-magnetic scattering (see Domke & Hubeny 1988). We then describe the assumptions leading us from this general form to simpler forms which are actually used in this paper. These details are scattered in several publications. Hence it is useful to list them here for the sake of clarity. The angle-dependent Domke-Hubeny PRD matrix can be written (see Domke & Hubeny 1988) as

$$\hat{R}(\lambda, \lambda', \Theta, z) = \gamma_{\text{coh}} R_{\text{II}}(\lambda, \lambda', \Theta, z) \hat{P}(\Theta; W_{\text{eff}} = W_2) + (1 - \gamma_{\text{coh}}) R_{\text{III}}(\lambda, \lambda', \Theta, z) \hat{P}(\Theta; W_{\text{eff}} = k_c W_2). \quad (\text{A1})$$

The depth-dependent coherence fraction is defined as

$$\gamma_{\text{coh}} = \frac{\Gamma_R + \Gamma_I}{\Gamma_R + \Gamma_I + \Gamma_E}. \quad (\text{A2})$$

The collisional depolarization factor is defined as

$$k_c = \frac{\Gamma_R + \Gamma_I}{\Gamma_R + \Gamma_I + D^{(2)}} \frac{\Gamma_E - D^{(2)}}{\Gamma_E}, \quad (\text{A3})$$

where  $D^{(2)}$  is the rate of depolarizing elastic collisions. The factor  $W_2$  in Equation (A1) depends on the angular momentum quantum numbers  $J_l$  and  $J_u$  of the lower and upper states, respectively. Note that  $W_2 = 1$  for the Ca I 4227 Å line.  $R_{\text{II}}$  and  $R_{\text{III}}$  are the scalar redistribution functions of Hummer (1962).  $\hat{P}(\Theta)$  is the scattering phase matrix (see Bommier 1997). The scattering angle  $\Theta$  is given by

$$\cos \Theta = \mu \mu' + \sqrt{(1 - \mu^2)(1 - \mu'^2)} \cos(\varphi' - \varphi), \quad (\text{A4})$$

where  $\mu = \cos \theta$  and  $\mu' = \cos \theta'$  represent the inclinations of the outgoing and incoming rays and  $\varphi$  and  $\varphi'$  are the respective azimuths in the atmospheric coordinate system fixed to the planar slab atmosphere, in which the scattering is described (see Figure 8).

For the axisymmetric (azimuthally independent) RT, the redistribution matrix can be written as

$$\hat{R}(\lambda, \lambda', \mu, \mu', z) = \frac{1}{2\pi} \int_0^{2\pi} \hat{R}(\lambda, \lambda', \Theta, z) d(\varphi' - \varphi). \quad (\text{A5})$$

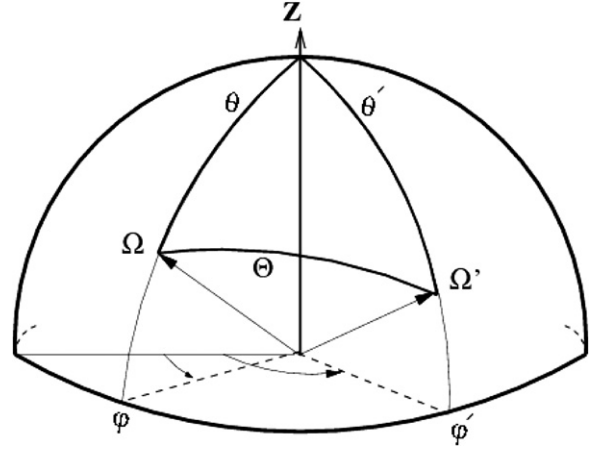


**Figure 8.** Scattering geometry.  $\Omega'$  and  $\Omega$  define the directions of the incoming and outgoing beams, respectively.  $\Theta$  is the scattering angle. The  $z$ -axis is along the atmospheric normal.

We make the approximation

$$\begin{aligned} \hat{R}(\lambda, \lambda', \mu, \mu', z) &= \gamma_{\text{coh}} R_{\text{II}}(\lambda, \lambda', \mu, \mu', z) \hat{P}(\mu, \mu'; \\ W_{\text{eff}} &= W_2) + (1 - \gamma_{\text{coh}}) R_{\text{III}}(\lambda, \lambda', \mu, \mu', z) \\ \hat{P}(\mu, \mu'; W_{\text{eff}} &= k_c W_2). \end{aligned} \quad (\text{A6})$$

In writing this expression, we assume that the azimuthal average of the redistribution matrix can be replaced by the product of the azimuthal averages of the redistribution functions and of the phase matrix. A similar factorization leads to the so-called hybrid approximation for PRD suggested by Rees & Saliba (1982). Averaging the redistribution functions in Equation (A6) over the scattering angle (defined by the angles  $\theta$  and  $\theta'$ ), one recovers the usual angle-averaged redistribution matrix

$$\hat{R}(\lambda, \lambda', \mu, \mu', z) = \gamma_{\text{coh}} R_{\text{II}}(\lambda, \lambda', z) \hat{P}(\mu, \mu'; W_{\text{eff}} = W_2) + (1 - \gamma_{\text{coh}}) R_{\text{III}}(\lambda, \lambda', z) \hat{P}(\mu, \mu'; W_{\text{eff}} = k_c W_2), \quad (\text{A7})$$

where

$$R_{\text{II,III}}(\lambda, \lambda', z) = \frac{1}{2} \int_0^\pi R_{\text{II,III}}(\lambda, \lambda', \Theta, z) \sin \Theta d\Theta \quad (\text{A8})$$

(see Equation (103) in Bommier 1997, and the averaging method in Hummer 1962; Mihalas 1978). Equation (A7), which is the hybrid approximation of Rees & Saliba (1982), is used in this paper and in most of the work with PRD (see, e.g., Faurobert-Scholl 1992; Nagendra 1994; Holzreuter et al. 2005; Sampoorana & Trujillo Bueno 2010). To recover the CRD limit, we set  $\gamma_{\text{coh}} = 0$ ; replace  $R_{\text{III}}(\lambda, \lambda', z) = \phi(\lambda, z)\phi(\lambda', z)$ , and also set  $(\Gamma_E - D^{(2)})/\Gamma_E = 1$  in the expression for  $k_c$ . The limit of frequency coherent scattering in the laboratory frame can be recovered by setting  $\gamma_{\text{coh}} = 1$  and through a replacement  $R_{\text{II}}(\lambda, \lambda', z) = \delta(\lambda - \lambda')\phi(\lambda', z)$ .

The scattering phase matrix is given by

$$\hat{P}(\mu, \mu'; W_{\text{eff}}) = \hat{P}^{(0)} + W_{\text{eff}} \hat{P}^{(2)}(\mu, \mu'), \quad (\text{A9})$$

which goes to the Rayleigh phase matrix  $\hat{P}_R$  when  $W_{\text{eff}}$  is set equal to unity.  $\hat{P}^{(0)}$  and  $\hat{P}^{(2)}$  are the multipolar components of the scattering phase matrix. They are written as

(Stenflo 1994)

$$\hat{\mathbf{P}}^{(0)} = \begin{pmatrix} 1 & 0 \\ 0 & 0 \end{pmatrix}; \quad \hat{\mathbf{P}}^{(2)}(\mu, \mu') \\ = \frac{3}{8} \begin{pmatrix} \frac{1}{3}(1-3\mu^2)(1-3\mu'^2) & -(1-3\mu^2)(1-\mu'^2) \\ -(1-\mu^2)(1-3\mu'^2) & 3(1-\mu^2)(1-\mu'^2) \end{pmatrix}. \quad (\text{A10})$$

*Redistribution matrix for the microturbulent magnetic fields.*

In this paper, we also use the microturbulent magnetic-field-averaged redistribution matrices. These matrices are found to be necessary in order to reproduce the core peak amplitude in the  $Q/I$  spectra of the Ca I 4227 Å line. The relevant redistribution matrix can be obtained simply by replacing  $W_{\text{eff}}$  by  $W_{\text{eff}} f_B$ , where

$$f_B = \begin{cases} 1 - \frac{2}{5} \left[ \frac{\gamma_h^2}{1+\gamma_h^2} + \frac{4\gamma_h^2}{1+4\gamma_h^2} \right] & \text{for } (\lambda, \lambda') \text{ in the line core} \\ 1 & \text{elsewhere,} \end{cases} \quad (\text{A11})$$

for the particular case of isotropic angular distribution of the microturbulent magnetic field (Stenflo 1982; Faurobert-Scholl 1993). The Hanle gamma parameter in the above equation is given by

$$\gamma_h = 0.88 g_J \frac{B_{\text{turb}}}{\Gamma_R + D^{(2)}}. \quad (\text{A12})$$

Here,  $B_{\text{turb}}$  is the magnetic field strength in Gauss and  $g_J$  is the Landé  $g$  factor of the upper level ( $g_J = 1$  for the Ca I 4227 Å line).  $\Gamma_R$  and  $D^{(2)}$  are expressed here in units of  $10^7 \text{ s}^{-1}$ .

## REFERENCES

- Avrett, E. H. 1995, in *Infrared Tools for Solar Astrophysics: What's Next?* ed. J. R. Kuhn & M. J. Penn (Singapore: World Scientific), 303
- Barklem, P. S., & O'Mara, B. J. 1997, *MNRAS*, **290**, 102
- Belluzzi, L., Trujillo Bueno, J., & Landi Degl'Innocenti, E. 2007, *ApJ*, **666**, 588
- Bianda, M., Ramelli, R., & Gisler, D. 2009, in *ASP Conf. Ser. 405, Solar Polarization 5*, ed. S. V. Berdyugina, K. N. Nagendra, & R. Ramelli (San Francisco, CA: ASP), 17
- Bianda, M., Stenflo, J. O., Gandorfer, A., & Gisler, D. 2003, in *ASP Conf. Ser. 286, Current Theoretical Models and Future High Resolution Solar Observations: Preparing for ATST*, ed. A. A. Pevtsov & H. Uitenbroek (San Francisco, CA: ASP), 61
- Bommier, V. 1997, *A&A*, **328**, 726
- Derouich, M., Sahal-Br  chot, S., Barklem, P. S., & O'Mara, B. J. 2003, *A&A*, **404**, 763
- Domke, H., & Hubeny, I. 1988, *ApJ*, **334**, 527
- Faurobert, M. 1987, *A&A*, **178**, 269
- Faurobert, M. 1988, *A&A*, **194**, 268
- Faurobert, M., & Arnaud, J. 2002, *A&A*, **395**, 305
- Faurobert-Scholl, M. 1992, *A&A*, **258**, 521
- Faurobert-Scholl, M. 1993, *A&A*, **268**, 765
- Faurobert-Scholl, M. 1994, *A&A*, **285**, 655
- Fluri, D. M., Holzreuter, R., Klement, J., & Stenflo, J. O. 2003, in *ASP Conf. Ser. 307, Solar Polarization III*, ed. J. Trujillo-Bueno & J. S  nchez Almeida (San Francisco, CA: ASP), 263
- Fontenla, J. M., Avrett, E. H., & Loeser, R. 1993, *ApJ*, **406**, 319
- Frisch, H., Anusha, L. S., Sampoorna, M., & Nagendra, K. N. 2009, *A&A*, **501**, 335
- Gandorfer, A. 2000, *The Second Solar Spectrum, Vol. I: 4625   to 6995  * (Zurich: vdf Hochschulverlag)
- Gandorfer, A. 2002, *The Second Solar Spectrum, Vol. II: 3910   to 4630  * (Zurich: vdf Hochschulverlag)
- Gandorfer, A. 2005, *The Second Solar Spectrum, Vol. III: 3160   to 3915  * (Zurich: vdf Hochschulverlag)
- Gandorfer, A. M., et al. 2004, *A&A*, **422**, 703
- Holzreuter, R., Fluri, D. M., & Stenflo, J. O. 2005, *A&A*, **434**, 713
- Holzreuter, R., Fluri, D. M., & Stenflo, J. O. 2006, *A&A*, **449**, L41
- Hummer, D. G. 1962, *MNRAS*, **125**, 21
- Mihalas, D. 1978, *Stellar Atmosphere* (2nd ed.; San Francisco, CA: Freeman)
- Nagendra, K. N. 1994, *ApJ*, **432**, 274
- Nagendra, K. N., Frisch, H., & Faurobert, M. 2002, *A&A*, **395**, 305
- Rees, D. E., & Saliba, G. J. 1982, *A&A*, **115**, 1
- Sampoorna, M., Nagendra, K. N., & Stenflo, J. O. 2007, *ApJ*, **670**, 1485
- Sampoorna, M., Stenflo, J. O., Nagendra, K. N., Bianda, M., Ramelli, R., & Anusha, L. S. 2009, *ApJ*, **699**, 1650 (S09)
- Sampoorna, M., & Trujillo Bueno, J. 2010, *ApJ*, **712**, 1331
- Stenflo, J. O. 1980, *A&A*, **84**, 68
- Stenflo, J. O. 1982, *Sol. Phys.*, **80**, 209
- Stenflo, J. O. 1994, *Solar Magnetic Fields: Polarized Radiation Diagnostics* (Dordrecht: Kluwer)
- Stenflo, J. O. 2005, *A&A*, **429**, 713
- Uitenbroek, H. 2001, *ApJ*, **557**, 389